ACCSCIENCE PUBLISHING

International Journal of Bioprinting

RESEARCH ARTICLE

Three-dimensional-printed porous titanium scaffolds outperform biphasic calcium phosphate ceramics for load-bearing critical-sized bone defect repair

Zijian Li[1,2†], Chenliang Quan[2,3†], Guanglin Wang[1,2†], Xiao Liu[1,2], Hufei Wang[1,2], Jianpeng Gao[1,2], Zhengyang Chang[1,2,4], Jiazhi Yan[1,2,4], Hua Chen[1,2*], Ming Li[1,2*], and Jianheng Liu[1,2*]

[1]Department of Orthopaedics, The Fourth Medical Center of the Chinese PLA General Hospital, Beijing, China

[2]Department of Orthopaedics, National Clinical Research Center for Orthopedics, Sports Medicine & Rehabilitation, Beijing, China

[3]Department of Orthopaedics, The First Medical Center of the Chinese PLA General Hospital, Beijing, China

[4]Department of Orthopaedics, Medical School of Chinese PLA, Beijing, China

(This article belongs to the *Special Issue: 3D Printing and Bioprinting Technologies for Bone Repair and Regeneration*)

[†]*These authors contributed equally to this work.*

***Corresponding authors:**
Hua Chen
(chenhua0270@126.com)
Ming Li
(liming891215@163.com)
Jianheng Liu
(jianhengliu@126.com)

Citation: Li Z, Quan C, Wang G, *et al*. Three-dimensional-printed porous titanium scaffolds outperform biphasic calcium phosphate ceramics for load-bearing critical-sized bone defect repair. *Int J Bioprint*. 2026;12(3):026180160. doi: 10.36922/IJB026180160

Received: April 29, 2026

Revised: June 6, 2026

Accepted: June 7, 2026

Published online: June 8, 2026

Abstract

Repairing critical-sized, load-bearing bone defects remains a formidable clinical challenge, primarily due to the mechanical fragility of traditional bioceramics. This study systematically compared the bone regenerative efficacy of surface-microstructured three-dimensional (3D)-printed porous titanium (3D-SMPT) and reinforced biphasic calcium phosphate (RBCP) ceramics. *In vitro* evaluations demonstrated that a biomimetic coating effectively overcame titanium's bioinertness, thereby endowing 3D-SMPT with excellent biocompatibility and osteoinductivity comparable to those of RBCP. *In vivo* cross-species assessments revealed significant biomechanical differences: in a low-load rabbit ulnar model, both scaffolds exhibited equivalent osteogenesis. However, in a true weight-bearing beagle femoral model, RBCP suffered severe structural collapse due to inherent brittleness. In stark contrast, leveraging its cortical bone-matched compressive strength (83.14 MPa, approximately 10-fold higher than that of RBCP at 7.68 MPa) and interconnected porosity, 3D-SMPT maintained long-term mechanical stability, effectively mitigating stress shielding to facilitate massive mature bone ingrowth and robust osseointegration. In conclusion, 3D-SMPT achieves a perfect integration of bioactivity and load-bearing stability, overcoming the inherent fragility of traditional ceramics and offering a highly promising clinical alternative for the repair of massive load-bearing bone defects.

Keywords: Three-dimensional printing; Porous titanium scaffold; Biphasic calcium phosphate; Microstructural modification; Bone regeneration

1. Introduction

Large bone defects from trauma, infection, and osteoporotic fractures have become more common due to fast societal modernization and an aging population.[1-3] The clinical treatment for these severe conditions is often long and difficult, with unpredictable outcomes.[4,5] In fact, due to the limitations of current treatments, approximately 5% to 10% of bone injuries worldwide eventually develop into permanent bone defects.[1] Currently, standard treatments for bone defects rely heavily on autologous and allogeneic bone grafts. Although autografts are widely considered the "gold standard," their application is restricted by a shortage of donor bone and the trauma of a second surgery.[6,7] Similarly, allografts face several challenges, including immune rejection, potential infection risks, and ethical concerns.[8,9] Together, these limitations restrict the widespread clinical use of traditional bone grafting methods. As a result, there is a pressing clinical need to investigate novel approaches to bone regeneration that might address the drawbacks of conventional treatments.

In the past few years, the rapid development of bone tissue engineering has supplied new approaches for the clinical treatment of bone defects.[10-13] As an important part of bone tissue engineering, synthetic biomaterials have received much attention. Among them, clinical practice has extensively used calcium phosphate (CaP) ceramics due to their similarity to natural bone and inorganic composition, which provide excellent biocompatibility, osteoconductivity, and osteoinductivity.[14-16] Currently, mainstream CaP-based bone graft materials mainly comprise β-tricalcium phosphate (β-TCP), hydroxyapatite (HA), and their biphasic combination (BCP).[17,18] Notably, BCP stands out for repairing large bone defects due to its strong osteoinductive capacity and an adjustable degradation rate that closely matches the bone formation process.[19,20] Clinical comparative studies have shown that when BCP ceramics and autologous iliac bone were implanted on opposite sides of the same patient's spine, they showed similar effects in promoting new bone formation.[21] In addition, Zhu *et al.*[22] altered the surface of BCP scaffolds with biomimetic microstructures, thereby enhancing the material's bioactivity and osteogenic efficiency. However, BCP still confronts significant clinical difficulties when used to repair substantial load-bearing bone defects. On the one hand, the inherent high brittleness of ceramics limits their mechanical strength.[23,24] On the other hand, in the initial phase of bone reconstruction, the mechanical strength of the newly formed tissue is insufficient to make up for the loss of support caused by the degradation of the scaffold.[25] This greatly increases the risk of mechanical failure at the implant site.

To overcome these mechanical bottlenecks, metallic biomaterials with excellent mechanical properties have evolved into a crucial option for repairing load-bearing bone defects.[25-27] Among them, titanium and its alloys are extensively utilized in clinical practice because of their exceptional biocompatibility, high strength, corrosion resistance, and low density.[28,29] In particular, porous titanium scaffolds fabricated by three-dimensional (3D) printing technology can not only provide immediate mechanical stability at the defect site, but also guide the ingrowth of adjacent bone tissue, ultimately achieving firm osseointegration between the host bone and the implant.[30,31] Meanwhile, the structure with pores effectively reduces the elastic modulus of the material, alleviating bone resorption caused by the stress shielding effect.[32-34] However, titanium alloys are inherently bioinert and non-degradable.[35] Therefore, enhancing their surface bioactivity to ensure the stability throughout time of the implant-bone interface is highly crucial. Previous studies have confirmed that chemically treated porous titanium may exhibit outstanding bioactivity and osteoinductive potential, while achieving high interfacial bonding strength.[36,37] Furthermore, if combined with simulated body fluid deposition, it can greatly improve mesenchymal stem cells' (MSCs) capacity to produce osteogenic differentiation.[38,39] Therefore, surface-bioactivated 3D-printed porous titanium is regarded as a highly promising candidate for repairing load-bearing bone defects. Although microstructure-modified BCP ceramics and surface-activated porous titanium scaffolds have shown great potential in their respective fields, few studies have directly and systematically compared these two representative scaffold materials for repairing load-bearing bone defects. It remains unclear whether the early *in vitro* bioactivity and osteoinductive performance of microstructure-modified porous titanium scaffolds can reach or even exceed those of modified BCP ceramics. Moreover, their bone-regeneration performance in actual *in vivo* load-bearing environments needs further clarification.

In this study, we comprehensively analyzed the regeneration capabilities of these two materials in load-bearing bone defects (Figure 1). We fabricated microstructure-modified reinforced BCP (RBCP) ceramics via hydrothermal synthesis, and surface-microstructured 3D-printed porous titanium (3D-SMPT) scaffolds using combined chemical and electrochemical deposition. *In vitro*, their bioactivities were compared by co-culturing with MSCs to assess cell proliferation and gene expression. *In vivo*, to overcome the clinical limitations of rodents lacking Haversian remodeling, we utilized critical-sized defect models in beagle femurs and rabbit ulnas. By closely mirroring human anatomical and physiological conditions,

this approach enables a highly realistic comparison of the osteogenic capabilities and clinical potential of 3D-SMPT versus RBCP scaffolds.

2. Materials and methods

2.1. Preparation of reinforced biphasic calcium phosphate

The BCP powder and BCP nanoparticle slurry used in this study were supplied by the National Engineering Research Centre for Biomaterials at Sichuan University (China). Initially, porous BCP scaffolds were fabricated utilizing an H_2O_2-based foaming technique according to a previously described method,[40] followed by a sintering process at 1,100 °C for two hours. Next, the dry and clean scaffolds were placed in a Teflon-lined hydrothermal autoclave containing a 1 mol/L nitric acid solution (pH = 6.0) at a solid-to-liquid ratio of 1:30. After sealing, the autoclave was heated to 200 °C for four hours. The hydrothermally treated scaffolds were collected after naturally cooling to room temperature. They were then progressively cleaned with deionized water and 100% ethanol before being dried for 24 h at 60 °C. Subsequently, a prepared BCP nanoparticle slurry (30 mg/mL) was introduced into the

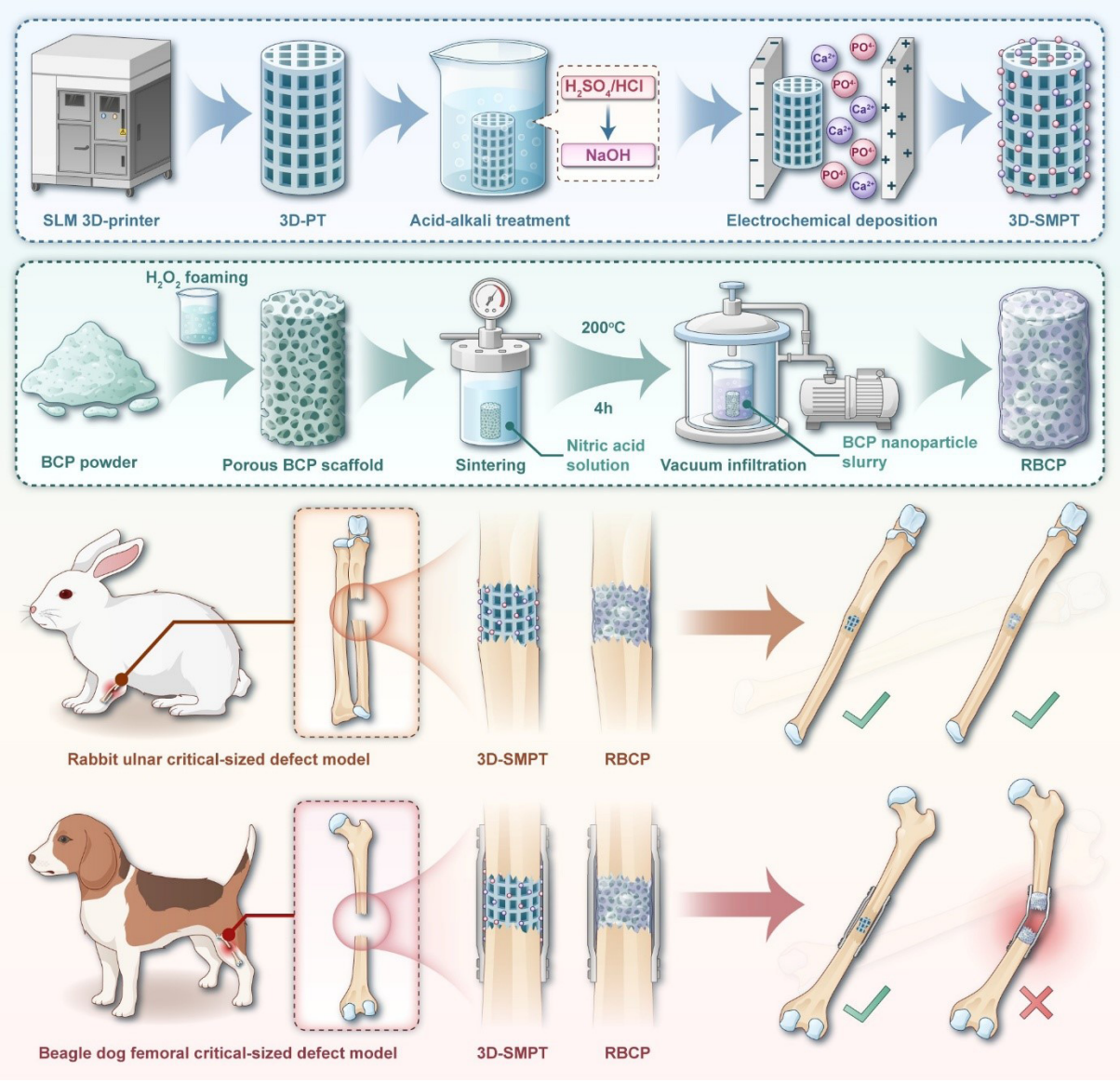

Figure 1. Schematic illustration of surface-microstructured three-dimensional-printed porous titanium (3D-SMPT) and reinforced biphasic calcium phosphate (RBCP) scaffolds for load-bearing bone defect repair

porous scaffold via vacuum infiltration. After drying, these infiltrated scaffolds were calcined at 1,100 °C. To yield the final microstructure-modified BCP ceramics (RBCP), this vacuum infiltration procedure was repeated using a 50% diluted suspension, followed by a final sintering step at 1,000 °C.

2.2. Preparation of three-dimensional-printed porous titanium

Xi'an, China's Northwest Institute for Non-ferrous Metal Research supplied the pre-alloyed Ti–6Al–4V powders used in this investigation, which ranged in particle size from 15 to 45 μm. Using a Renishaw (United States) AM 400 system and selective laser melting, cylindrical porous Ti–6Al–4V scaffolds measuring 5 mm in diameter and 12 mm in height were created. Based on models generated with computer-aided design software (123D Design, version 2.2), the specimens were built by selectively melting designated regions of the powder bed layer per layer. The porous structure was designed using a diamond-type lattice unit cell with a strut diameter of 400 μm and a designed pore size of approximately 600 μm. The scaffolds were fabricated with a target porosity of 66.0% and fully interconnected pores to facilitate vascular ingrowth and nutrient transport. A maximum laser power of 400 W, a laser spot diameter of roughly 70 μm, and a powder layer thickness of 30 μm were among the manufacturing characteristics. For pretreatment, the as-built samples were successively ultrasonically cleaned in petroleum ether, acetone, absolute ethanol, and deionized water (3 times, 10 min per cycle), and then dried. To construct a roughened surface topography and introduce hydroxyl groups, the samples underwent an acid–alkali treatment. They were first immersed in a mixed acid solution (98% sulfuric acid, 34% hydrochloric acid, and deionized water with a 1:1:2 volume ratio) at 70 °C for one hour. Following a deionized water rinse, the samples were submerged in a solution of 6 M sodium hydroxide at 70 °C for five hours, then succeeded by washing to a neutral pH. For electrochemical deposition, an electrolyte containing calcium, phosphate, and sodium chloride ($[Ca^{2+}]$ = 2.5 mM, [P] = 1.5 mM, Ca/P = 1.67) was introduced into the micropores of the titanium substrates via vacuum infiltration. The deposition was performed in a glass cell using a standard three-electrode system, with the porous titanium serving as the cathode, a high-purity platinum plate as the anode, and a saturated calomel electrode. The electrolyte was heated in a water bath to 80 °C, and the deposition was driven by a pulsed current. Finally, the specimens were cleaned using deionized water until neutral.

2.3. Characterization

2.3.1. Scanning electron microscopy

A scanning electron microscope (SEM; JSM-6700F, Hitachi, Japan) was used to examine the surface morphologies of the RBCP and 3D-SMPT scaffolds. Prior to observation, a magnetron sputter coater (E-1010, Hitachi, Japan) was used to mount the RBCP and 3D-SMPT scaffolds onto specimen stubs using two-sided conductive tape and a gold sputter coating under vacuum (10^{-4} Pa). To ensure uniform deposition of the gold coating, the samples were rotated at 10 rpm during the process, with a voltage of 12 kV and a coating duration of 120 seconds. Furthermore, the porosity of the scaffolds was determined using the mass–volume method. Regular-shaped samples' mass and volume were properly measured, and the porosity was computed using the formulas $\rho = m/v$ and $P = 1 - \rho/\rho_0$, where ρ shows the scaffold's apparent density, m and v are the mass and volume of the sample, respectively; P is the porosity, and ρ_0 is the theoretical density of the bulk material. For every group, three samples in parallel were analyzed, and the average values were determined.

2.3.2. X-ray diffraction

The RBCP and 3D-SMPT scaffolds were prepared into disks with dimensions of Φ14 × 1 mm. An X-ray diffractometer (D8 Advance, Bruker, Germany) with Cu Kα radiation (λ = 1.5406 Å) running at 40 kV and 40 mA was used to investigate the samples' phase compositions. To determine the phases, the resulting diffraction patterns were compared with standard Joint Committee on Powder Diffraction Standards (JCPDS) cards for HA (JCPDS 09-0432), anatase (JCPDS 21-1272), titanium (JCPDS 05-0682), and β-TCP (JCPDS 09-0169).

2.3.3. Mechanical properties test

An electronic universal testing machine (3365 Instron, United States) was used to assess the scaffolds' compressive mechanical properties at room temperature. The specimens were prepared as cylinders with dimensions of Φ5 × 12 mm. A rate of loading of 1.0 mm/min was used for the compression testing, and three parallel measurements were carried out for each experimental group.

2.4. *In vitro* cytology testing

2.4.1. Cell culture

For every *in vitro* experiment, bone marrow-derived MSCs (BMSCs) from the PLA General Hospital's Orthopedic Laboratory (China) were used. The cells were grown

to passage 3 in α-Minimum Essential Medium (MEM) supplemented with 10% fetal bovine serum (FBS) and 1% penicillin–streptomycin. The nutritional medium was replaced every 48 hours, and the culture system was maintained at 37 °C in a humidified 5% carbon dioxide environment.

2.4.2. Extract preparation

The International Organization for Standardization's (ISO 10993-12:2021) guidelines were followed in the preparation of material extracts.[41] Prior to extraction, the RBCP and 3D-SMPT scaffolds were sterilized via Co-60 γ-irradiation. The experiment was separated into three groups: the RBCP extract group, the 3D-SMPT extract group, and a blank control group. The sterilized samples were fully submerged in α-MEM enhanced with 10% FBS and incubated for 72 h at 37 °C with 5% carbon dioxide in a humid atmosphere. For subsequent *in vitro* tests, the resulting extracts were collected and stored at 4 °C.

2.4.3. Cell Counting Kit-8 assay

Bone marrow-derived MSCs were cultured at a density of 1×10^3 cells/mL in a 96-well plate to assess cell proliferation (100 μL per well, with five duplicate wells for each group). The peripheral wells were filled with sterile PBS to prevent evaporation. The original medium was aspirated after incubation for 24 hours at 37 °C in 5% carbon dioxide to promote cell adhesion. The experimental groups were treated with equal volumes of their respective material extracts, while the control group was treated with fresh α-MEM containing 10% FBS. Cell proliferation was evaluated on days 1, 3, and 5. At each predetermined time point, 10 μL of Cell Counting Kit-8 (CCK-8) solution was added into each well, and the mixture was incubated for a further two hours at 37 °C. Finally, a microplate reader was used to measure each well's optical density (OD) value at a wavelength of 450 nm.

2.4.4. Live/Dead staining

To evaluate cell viability, BMSCs were seeded into confocal dishes at a density of 1.0×10^4 cells/cm^2. Upon cell adhesion, the initial medium was replaced with the respective material extracts. On the first and third days of co-culture, the cells were stained with a Live/Dead cell staining kit (Beyotime, China) in strict accordance with the manufacturer's guidelines. Subsequently, a confocal laser scanning microscope was used to take fluorescence pictures of the labeled cells (LSM 880, ZEISS, Germany).

2.4.5. Cytoskeletal staining

Cytoskeleton staining was employed to evaluate the materials' *in vitro* cytocompatibility and cell morphology. In short, BMSCs were cultured for one day in extracts from the various experimental groups. After 15 minutes of 4% paraformaldehyde fixation, the cells underwent permeabilization using 0.1% Triton X-100. The cells were then sequentially stained with 4',6-diamidino-2-phenylindole for five minutes in the dark and with 1% Alexa Fluor 488 phalloidin (Beyotime, China) for 60 minutes. Lastly, a confocal laser scanning microscope was used to obtain fluorescence pictures of the labeled cells.

2.4.6. Alkaline phosphatase staining

Bone marrow-derived MSCs were seeded at a density of 2×10^2 cells/well onto 24-well plates to assess early osteogenic differentiation. Following cell adhesion, the original α-MEM was aspirated and substituted with medium extracts enriched with osteogenic induction agents. Cells were fixed with 4% paraformaldehyde (1 mL/well) for 30 minutes on days 7 and 14 of osteogenic induction. The plates were subsequently incubated at 37 °C in the dark for 30 minutes after 1 mL of alkaline phosphatase (ALP) staining solution (Beyotime, China) was included in each well. A stereomicroscope (SMZ25; Nikon, Japan) was used to examine and document the cells' ALP staining morphology following three PBS washes.

2.4.7. Alizarin Red S staining

Osteogenic induction and BMSC seeding were carried out in accordance with the procedure outlined in Section 2.4.6. Firstly, 4% paraformaldehyde was used to fix the cells (1 mL/well) for 30 minutes on days 14 and 21 of induction. The cells were then stained for 10 minutes at 37 °C using 1.5 mL of Alizarin Red S (ARS) staining solution (Beyotime, China). The development of calcified nodules was observed and photographed with a stereomicroscope (SMZ25; Nikon, Japan) after three PBS washes to remove excess dye. To elute the bound dye for quantitative analysis of calcium deposition, 10% cetylpyridinium chloride was used. Every experiment was carried out three times.

2.4.8. Real-time quantitative polymerase chain reaction

In 6-well plates, BMSCs (10×10^4 cells per well) were cultivated for a whole day. Then, different experimental extracts containing an osteogenic supplement were substituted for the medium. TRIzol Reagent (TRIzol™, Thermo Fisher Scientific, United States) was used to extract total cellular RNA after a three-day incubation period. Real-time quantitative polymerase chain reaction (RT-qPCR) was utilized to quantify the expression levels of osteocalcin (*OCN*) and osteopontin (*OPN*), and the sequences of specific forward and reverse primers used for target gene amplification were as follows:

(i) *OCN* forward: 5'-GGCAGCGAGGTAGTGAAGA-3'
(ii) *OCN* reverse: 5'-TCAGCCAACTCGTCACAGTC-3'
(iii) *OPN* forward: 5'-TCAGCGGATGACCAGAGTG-3'
(iv) *OPN* reverse: 5'-TTGGGGTCTACAACCAGCAT-3'

Three separate replicates of each sample were examined.

2.5. Biological testing *in vivo*

2.5.1. Critical-sized bone defect modeling

Every animal study adhered to guidelines sanctioned by the Ethics Committee of the PLA General Hospital (Approval No.: 2022-x18-51).

Thirty 6-month-old male New Zealand white rabbits (Animal Experimental Center of the PLA General Hospital, China) weighing 2.6 ± 1.3 kg were chosen and randomly assigned to the RBCP group, 3D-SMPT group, and control group (n = 10 per group) to establish the rabbit ulnar critical-sized defect model. The animals were fasted for 12 hours before the procedure. General anesthesia was induced using a combination of xylazine hydrochloride (0.1 mL/kg, i.m.) and 3% pentobarbital sodium (2 mL/kg, i.v.). A longitudinal incision was made at the mid-radius following standard cleaning and draping of the surgical site. A 12-mm segmental critical-sized bone defect was created using a bone cutter, and the periosteum in the defect area was thoroughly stripped and removed. The flaws were then filled with size-matched RBCP or 3D-SMPT scaffolds (Φ5 × 12 mm), whereas the control group was left empty. After confirming no active bleeding, the muscle and skin layers were sutured. To prevent infection after surgery, penicillin (400,000 U/day) was administered intramuscularly for three consecutive days.

For the establishment of the beagle dog femoral critical-sized defect model, 30 one-year-old healthy adult male beagle dogs (average weight 15 kg; supplied by the Animal Experimental Center of the PLA General Hospital, China) were allocated at random to the control group, RBCP group, and 3D-SMPT group (n = 10 per group). After inducing intravenous compound anesthesia, a longitudinal incision was applied to the right thigh's lateral side, and the mid-diaphysis of the femur was exposed through blunt dissection via the intermuscular space. Using an oscillating saw and constant saline irrigation for cooling, a 2-cm segmental bone defect was made 2.5 cm proximal to the distal femoral condyle. Following the implantation of RBCP or 3D-SMPT scaffolds, internal fixation was performed using a bone plate and screws (three screws each at the proximal and distal ends). Layer by layer, the incisions were sutured without external fixation. Antibiotics (penicillin and streptomycin) were routinely administered before and after surgery to prevent infection. The dogs were fed a high-protein diet, and sutures were removed 14 days post-surgery.

2.5.2. X-ray analysis

At 4, 8, and 12 weeks post-operative, radiographic analyses of the bone defect locations were performed in both beagle dogs and New Zealand rabbits. After anesthesia, the animals were positioned on the examination table in a lateral decubitus position, and the affected limbs were positioned for X-ray imaging. A tube voltage of 110 kV, a tube current of 75 mA, and an exposure duration of 0.15 seconds were chosen as the imaging parameters.

2.5.3. Micro-computed tomography analysis

A micro-computed tomography (CT) scanning system (Inveron MM, Siemens, Germany) was used to assess the extent of newly formed bone at the bone defect sites in both beagle dogs and New Zealand rabbits. The effective pixel size was 9.08 μm, the exposure length was 1,500 ms, the tube voltage was 75 kV, and the tube current was 400 μA. The Inveon Research Workplace software (Siemens, Germany; version 4.2) was used to recreate 3D images following scanning. Bone volume (BV), bone volume/total volume (BV/TV), and bone mineral density (BMD) were among the osteogenesis-related measures assessed within the region of interest.

2.5.4. Histology analysis

The specimens were embedded in poly(methyl methacrylate) after fixation in 4% paraformaldehyde and dehydration in a graded ethanol series (70–100%). A hard tissue microtome (Leica, Germany) was used to create longitudinal sections with an initial thickness of about 150 μm. Precision grinding and polishing procedures were then used to thin these pieces to approximately 40 μm. The morphological features of the developing tissue and the patterns of collagen deposition were then assessed using hematoxylin and eosin (H&E) and Masson's trichrome staining, respectively. Lastly, representative photos were taken for histological analysis after the target areas were examined under a light microscope (BX53, Olympus, Japan).

2.6. Statistical analysis

GraphPad Prism 10.1 was used for data processing and visualization. Initially, the Shapiro–Wilk test was used to determine whether the data distribution was normal. Mean ± standard deviation was used to display all quantitative results. The Mann–Whitney U test or the independent Student's t-test was chosen for two-group comparisons based on the data's distributional characteristics. One-way analysis of variance was used to assess significant differences among several groups, and Tukey's post hoc test was

employed for pairwise comparisons. Three independent replications of each experiment were conducted. $^{*}p < 0.05$, $^{**}p < 0.01$, and $^{***}p < 0.001$ were considered statistical significant.

3. Results

3.1. Characterization of reinforced biphasic calcium phosphate and surface-microstructured three-dimensional-printed porous titanium

As shown in the macroscopic photographs in Figure 2A, surface microstructural treatments of RBCP and 3D-SMPT were successfully achieved via hydrothermal treatment and chemical and electrochemical deposition methods, respectively. SEM images (Figure 2B) show that both scaffolds exhibited a porous network structure with uniform pore distribution, thin pore walls, and interconnected macropores. Measurements indicated that the pore size of 3D-SMPT varied from 400 μm to 500 μm, while that of RBCP ranged from 100 μm to 500 μm. Further high-magnification SEM images (Figure 2B) clearly displayed the characteristic surface morphologies of the 3D-SMPT and RBCP scaffolds, directly confirming the successful modification of their surface microstructures. The calculated porosities were 66.0 ± 0.7% for the 3D-SMPT scaffold and 74.6 ± 3.0% for the RBCP scaffold.

X-ray diffraction further confirmed the phase compositions of the fabricated 3D-SMPT and RBCP scaffolds. For 3D-SMPT (Figure 2C), characteristic diffraction peaks corresponding to titanium (PDF#05-0682), anatase (PDF#21-1272), and HA (PDF#09-0432) were detected. This indicated that the chemical and electrochemical deposition therapies successfully induced the formation of anatase and HA phases on the titanium framework, realizing the construction of a micro-structured composite bioactive coating on the 3D-printed porous titanium substrate. Similarly, the X-ray diffraction pattern of the RBCP scaffold (Figure 2D) exhibits a typical biphasic composition, with its diffraction peaks perfectly matching the standard cards of β-TCP and HA. This confirmed that the surface hydrothermal microstructural treatment successfully preserved the desired biphasic CaP structure without introducing any unwanted impurity phases.

The stress–strain curves from the mechanical property tests demonstrated that the two scaffolds exhibited completely different mechanical behaviors during compression. For the 3D-SMPT scaffold (Figure 2E), the compressive stress increased steadily with strain and entered an extended, gentle yield plateau after reaching its peak, demonstrating excellent compressive buffering capacity. Conversely, the stress of the RBCP scaffold (Figure 2F) dropped sharply immediately after reaching the peak stress, presenting typical characteristics of ceramic brittle fracture. Quantitative analysis (Figure 2G) revealed that the compressive strength of 3D-SMPT reached up to 83.14 ± 0.96 MPa, whereas that of the RBCP scaffold was 7.68 ± 0.23 MPa. According to statistical analysis, the 3D-SMPT scaffold's compressive strength was significantly greater than the RBCP scaffold's ($^{***}p < 0.001$).

3.2. Evaluation of *in vitro* biocompatibility

The proliferation of BMSCs was initially measured using a CCK-8 test to analyze the materials' *in vitro* cytotoxicity and their impact on cell proliferation. As shown in Figure 3A, at prolonged culture times (days 1, 3, and 5), cells from all groups showed a consistent tendency toward proliferation. Statistical analysis revealed that at any given time point, cell proliferation levels did not differ significantly among the RBCP, 3D-SMPT, and blank control groups, indicating that the extracts from both scaffold materials are non-cytotoxic. We further evaluated cell viability visually and quantitatively using Live/Dead fluorescence staining (Figure 3D). Following a day or three of culture, the majority of cells in all three groups showed significant green fluorescence, indicative of living cells, according to confocal microscopy images, while very few cells showed red fluorescence, indicative of dead cells. The live and dead cell counts for the RBCP and 3D-SMPT groups on days 1 and 3 were similar to those in the control group, with no statistically significant differences between the groups, according to quantitative analysis of the fluorescence images (Figure 3B and 3C). This further confirmed the materials' excellent *in vitro* cytocompatibility, collectively demonstrating non-cytotoxicity in accordance with ISO 10993 standards.[42]

Furthermore, to observe cell adhesion and morphological extension across different substrates, fluorescence staining of the cytoskeleton and nuclei was performed. According to Figure 3E, cells in all three groups exhibited healthy, well-spread morphologies. The green microfilament cytoskeleton labeled by phalloidin was highly developed in each group, forming distinct filopodia and lamellipodia structures, while the blue nuclei stained by 4',6-diamidino-2-phenylindole remained morphologically intact. The cell spreading behavior in the RBCP and 3D-SMPT groups was virtually identical to that of the control group, showing that both materials can provide a highly favorable microenvironment for the early adhesion, cytoskeletal assembly, and morphological extension of BMSCs.

3.3. Assessment of *in vitro* osteogenic differentiation

To thoroughly assess the scaffold materials' capacity

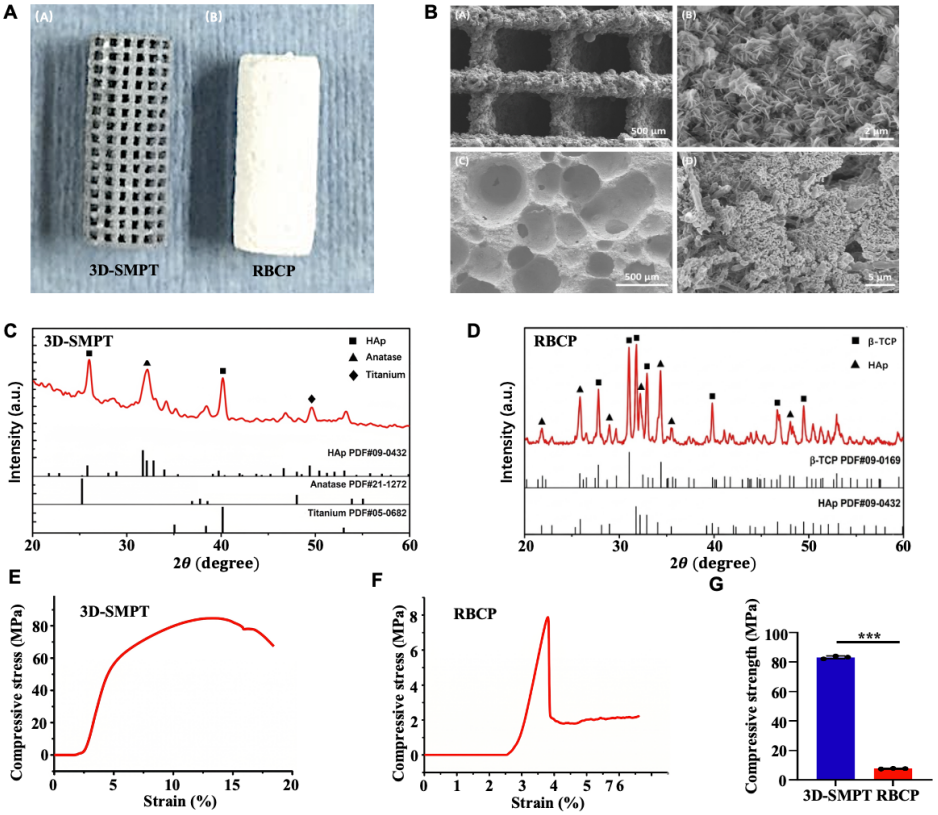

Figure 2. Characterization analysis. (A) The general morphology of 3D-SMPT and RBCP. (B) Scanning electron microscopy results for 3D-SMPT and RBCP. The porosity values of 3D-SMPT and RBCP are 66.0% and 74.6%, respectively. Scale bars: 2 μm, 5 μm, 500 μm; magnifications: 10,000×, 4,000×, 100×. (C) X-ray diffraction results of the 3D-SMPT. (D) X-ray diffraction results of the RBCP. (E) 3D-SMPT stress–strain curves. (F) RBCP stress–strain curves. (G) Compressive strength of RBCP and 3D-SMPT. The findings are shown as mean ± standard deviation ($n = 3$), with significance thresholds set at $^{*}p < 0.05$, $^{**}p < 0.01$, and $^{***}p < 0.001$.

Abbreviations: 3D-SMPT: Surface-microstructured three-dimensional-printed porous titanium; HAp: Hydroxyapatite; RBCP: Reinforced biphasic calcium phosphate.

for osteogenic differentiation *in vitro* on BMSCs, we systematically assessed early marker expression, late-stage matrix mineralization, and the transcriptional levels of genes associated with osteogenesis during the osteoinduction process. One important early indicator of osteogenic differentiation is ALP. As shown in Figure 4A, after induction culture for 7 and 14 days, ALP staining in both the RBCP and 3D-SMPT groups exhibited a deep blue-purple color, with the staining intensity and area increasing significantly over time. In contrast, the blank control group showed only extremely weak staining. The quantitative ALP activity assay (Figure 4B) further corroborated the staining results: at both time points, ALP activity in the RBCP and 3D-SMPT groups was considerably higher than in the control group ($^{**}p < 0.001$). Both groups showed strong early osteoinductive capacity, although the RBCP group's ALP activity was marginally higher than that of the 3D-SMPT group on day 14 ($p < 0.05$).

To evaluate extracellular matrix mineralization late in the osteogenic differentiation process, ARS staining and quantitative calcium content analysis were performed. As shown in the microscopic images in Figure 4D, after 14 and 21 days of culture, both the RBCP and 3D-SMPT groups exhibited abundant, dense, and deeply red-stained calcium nodules, whereas nodule formation in the control group was extremely scarce. The quantitative calcium content analysis (Figure 4C) was highly consistent with the morphological observations: at days 14 and 21, calcium deposition in both scaffold groups was substantially higher than in the blank control group, and RBCP and 3D-SMPT groups did not differ statistically. This indicates that 3D-SMPT possesses excellent efficacy in inducing late-stage mineralization comparable to that of RBCP.

Finally, we evaluated the expression of specific genes associated with osteogenesis at the molecular level using RT-qPCR. As presented in Figure 4E and 4F, in contrast to the blank control group, the mRNA expression levels of *OCN* (Figure 4E) and *OPN* (Figure 4F) in

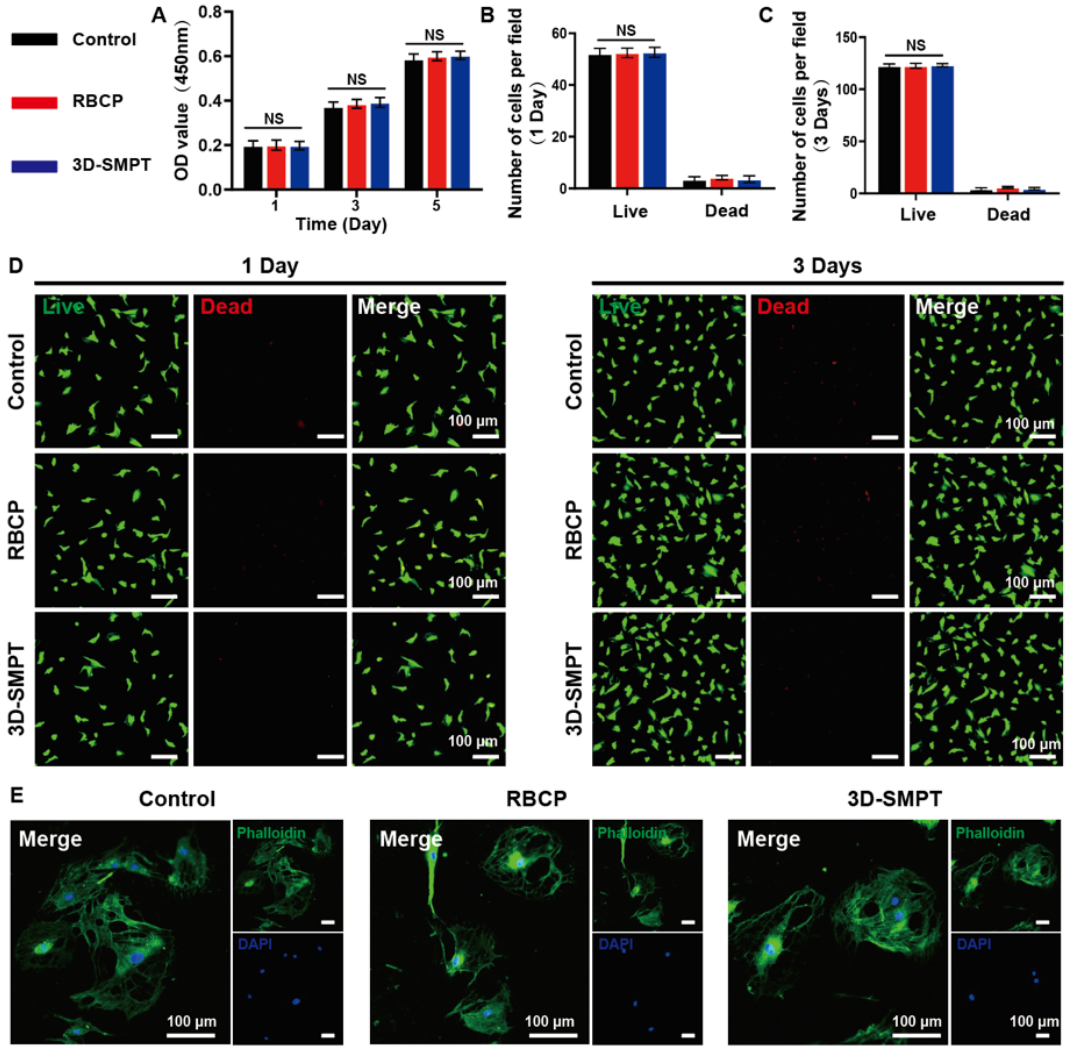

Figure 3. Testing for *in vitro* cytology. (A) The Cell Counting Kit-8 test was used to assess BMSC viability in each group on days 1, 3, and 5 ($n = 5$). (B) Quantitative examination of each group's living and dead cells on the first day ($n = 5$). (C) On day three, each group's live and dead cells were quantitatively analyzed ($n = 5$). (D) BMSCs in various groups were stained with Live/Dead staining on days 1 and 3. Living cells are represented by green, whereas dead cells are represented by red. Scale bar: 100 μm; magnification: 10×. (E) BMSCs in various groups stained with phalloidin after one day of culture. Scale bar: 100 μm; magnification: 10×. The mean ± standard deviation is used to express the data. NS stands for no significant difference.
Abbreviations: 3D-SMPT: Surface-microstructured three-dimensional-printed porous titanium; BMSC: Bone marrow-derived mesenchymal stem cell; OD: Optical density; RBCP: Reinforced biphasic calcium phosphate.

BMSCs cultured with RBCP and 3D-SMPT were highly significantly upregulated (**$p < 0.001$). The two scaffold groups were equally effective in promoting the expression of these core osteogenic genes. Taken together, these outcomes demonstrate that the 3D-SMPT scaffold not only possesses excellent biocompatibility but also exhibits robust *in vitro* osteoinductive activity comparable to that of traditional bioceramics.

3.4. Assessment of *in vivo* bone repair in a critical-sized rabbit ulnar defect model

As depicted in Figure 5A, the establishment of a rabbit ulnar critical-sized bone defect model was accomplished, and RBCP and 3D-SMPT scaffolds were implanted into the defect areas, respectively. Radiographic images at 4, 8, and 12 weeks following surgery (Figure 5B) fully documented the progression of bone healing in each group. In the control group, only trace amounts of callus formed at 4 weeks; by 8 and 12 weeks, although callus volume and density had slightly increased, the defect remained open, presenting a typical pathological image of non-union. In contrast, the RBCP group exhibited low-density callus formation as early as 4 weeks. By 8 weeks, the callus volume increased significantly, and the medial cortical bone outline

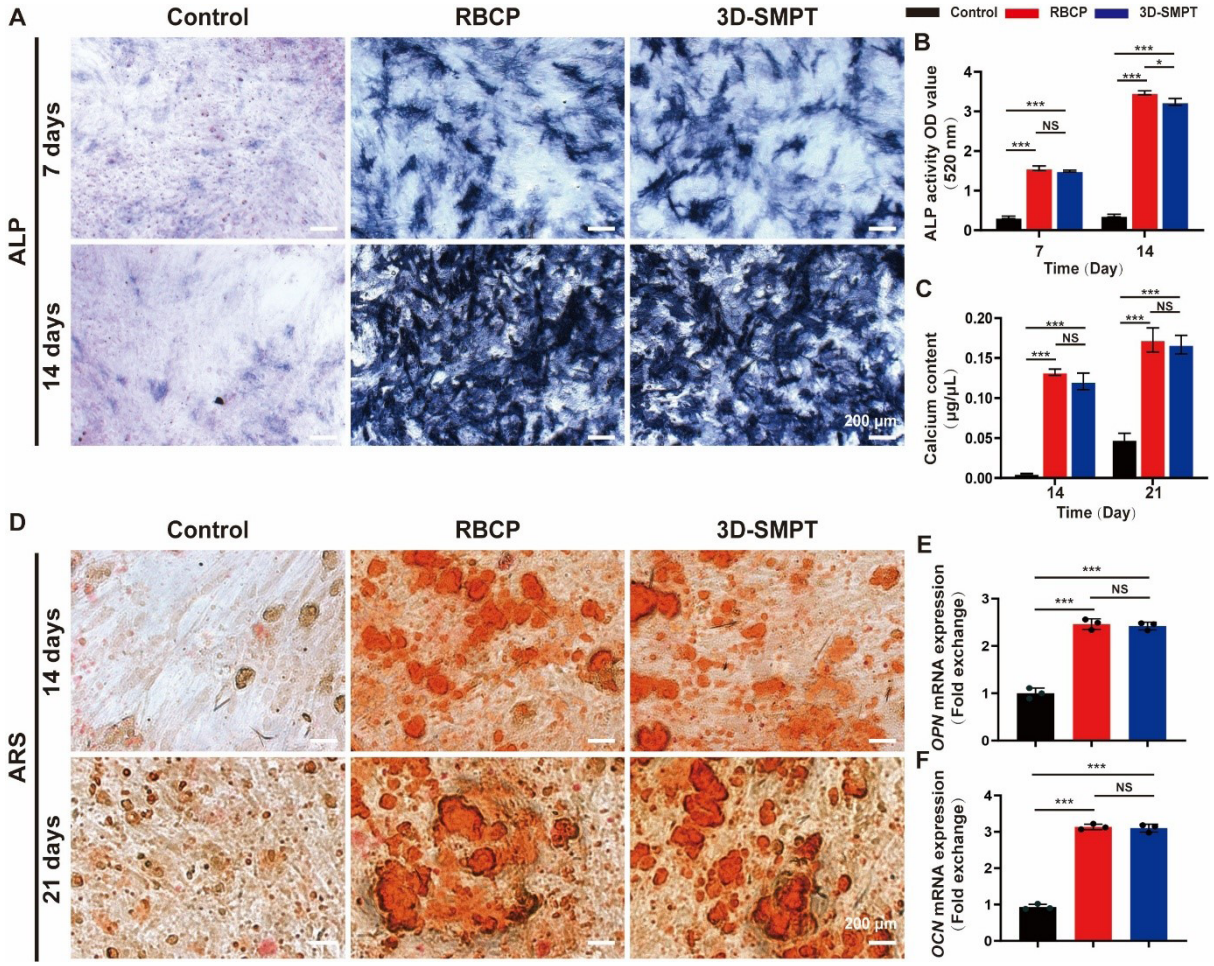

Figure 4. Testing for *in vitro* osteoinduction. (A) Alkaline phosphatase (ALP) staining at 7 and 14 days was visible in representative stereomicroscope pictures. Scale bar: 200 μm; magnification: 4×. (B) Quantitative analysis of ALP activity. (C) Quantitative analysis of calcium content. (D) Alizarin Red S (ARS) staining at 14 and 21 days was visible in representative stereomicroscope pictures. Scale bar: 200 μm; magnification: 4×. (E) On the third day of the experiment, the expression levels of genes associated with osteogenesis were measured by real-time quantitative polymerase chain reaction (*OCN*, *OPN*). Mean ± standard deviation ($n = 3$) is used to express the results. *$p < 0.05$, *$p < 0.01$, ***$p < 0.001$, and NS stands for no significant difference.
Abbreviations: 3D-SMPT: Surface-microstructured three-dimensional-printed porous titanium; OD: Optical density; RBCP: Reinforced biphasic calcium phosphate.

became preliminarily visible. By 12 weeks, the defect area achieved bony union, the callus entered the remodeling phase, and the freshly created bone's density tended to be uniform. Notably, the 3D-SMPT group demonstrated an excellent repair efficacy highly consistent with that of the RBCP group. At four weeks, the scaffold's contact with the host bone had developed a partial callus. By 8 weeks, the interfacial callus volume increased substantially, achieving preliminary bony union. By 12 weeks, the callus similarly entered the remodeling stage with a uniform density tendency.

To further assess the 3D microstructure of the newly formed bone, micro-CT scanning and reconstruction were performed on the samples at 12 weeks post-operation (Figure 5C). The visual images demonstrated that the osteogenic efficacy of both experimental groups was far greater than that of the control group: at 12 weeks, the control group showed occasional formation osseuse at the medial edges, with the defect still clearly visible; in contrast, both the RBCP and 3D-SMPT groups successfully bridged the two ends of the defect with an abundance of new bone tissue growing into the defect areas. BMD, BV/TV, and trabecular number were all considerably higher in the RBCP and 3D-SMPT groups than in the control group, according to quantitative bone morphometric examination of the defect area (Figure 5D–F) (*$p < 0.05$, ***$p < 0.001$). Importantly, none of the previously listed fundamental osteogenic markers showed statistically significant variations between the RBCP and 3D-SMPT

groups. Taken together, the radiological observations and quantitative analyses demonstrate that, in the low-weight-bearing rabbit ulnar defect model, the 3D-SMPT scaffold exhibits an excellent *in vivo* osteogenic repair capability comparable to the RBCP scaffold.

3.5. Radiological and micro-computed tomography evaluation of *in vivo* bone repair in a beagle dog model

As depicted in Figure 6A, a model of a critical-sized femoral defect in a large animal (beagle dog) was successfully established. After stabilizing the fracture ends with an internal fixation plate, the respective scaffolds were implanted into the defect area to evaluate their bone repair capabilities in a true weight-bearing environment. Radiographic images at 0H, 4W, 8W, and 12W post-operation (Figure 6B) fully recorded the progression of bone healing and mechanical maintenance. Throughout the experimental period, none of the implants triggered obvious signs of rejection or local infection, demonstrating excellent clinical biocompatibility. At four weeks, only trace callus formation was seen in the control group. Although a small amount of callus grew slowly toward the center at 8 and 12 weeks, a distinct radiolucent gap remained at 12 weeks, presenting a typical non-union outcome.

Notably, under weight-bearing conditions, the RBCP and 3D-SMPT groups exhibited starkly different mechanical stabilities and repair outcomes. The RBCP group showed some osteogenic activity in the early postoperative period (4 weeks), with rough and blurred images of newly

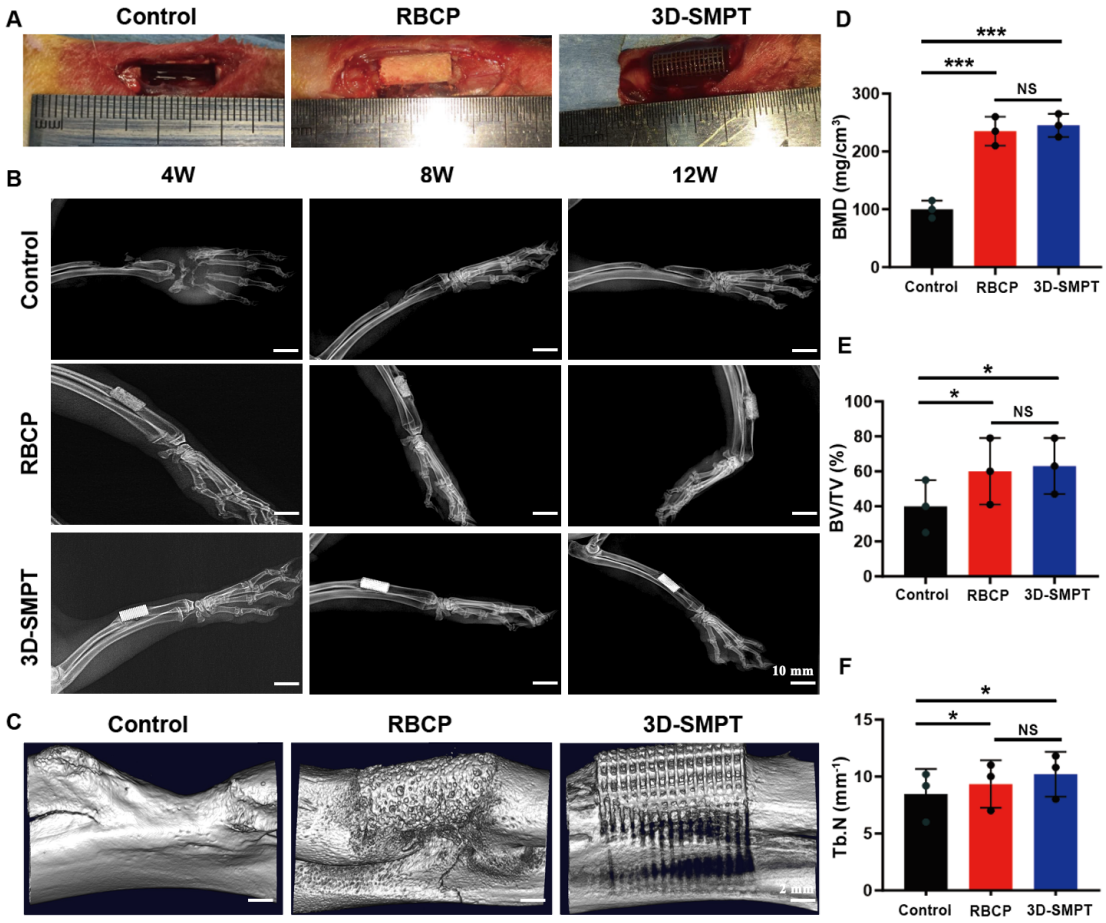

Figure 5. A rabbit ulnar critical-sized defect model is used to evaluate *in vivo* bone defect healing. (A) Macroscopic surgical photographs showing the creation of the defect and the implantation of scaffolds. (B) Radiographic images showing the progression of bone healing at four, eight, and twelve weeks following surgery. Scale bar: 10 mm. (C) Micro-computed tomography (CT) three-dimensional reconstruction images of the freshly grown bone in the location of the deformity at 12 weeks post-operation. Scale bar: 2 mm. (D–F) Quantitative microarchitectural examination of the regenerated bone at 12 weeks after surgery using micro-CT data: trabecular number (Tb.N), bone mineral density (BMD), and bone volume fraction (BV/TV). The findings are presented as mean ± standard deviation ($n = 3$), with significance thresholds set at $^{*}p < 0.05$, $^{**}p < 0.01$, and $^{***}p < 0.001$; NS refers to non-significant. Abbreviations: 3D-SMPT: Surface-microstructured three-dimensional-printed porous titanium; RBCP: Reinforced biphasic calcium phosphate.

formed callus visible around the scaffold. However, as time progressed and the affected limb's weight-bearing activity increased, the inherent disadvantages of the RBCP ceramic scaffold—high brittleness and insufficient mechanical strength—became fully apparent. Radiographic tracking and postoperative CT images (Figure 6B and 6C) clearly revealed that by 8 and 12 weeks, the RBCP scaffold had severely collapsed and fractured, completely losing its stress-bearing capacity, which subsequently led to obvious bending and deformation of the originally straight internal fixation plate. Although high-density callus formed near the fracture ends, this mechanical failure directly triggered an angular deformity of the affected limb, not only severely delaying the healing process but ultimately resulting in malunion.

In sharp contrast, the 3D-SMPT group perfectly maintained its straight macroscopic anatomical morphology and stability throughout the 12-week observation period. Using porous titanium's exceptional compressive strength, the 3D-SMPT scaffold underwent no deformation or fracture. It effectively shared the mechanical load of the internal fixation plate and successfully guided the continuous, uniform ingrowth of new bone tissue along its porous framework. Micro-CT two-dimensional slice images at 12 weeks post-operation (Figure 6C) further corroborated this: the titanium mesh structure of the 3D-SMPT group remained absolutely intact, the bone tissue bonded tightly with the metal interface, and no material degradation or mechanical detachment was observed. A dense, continuous callus had formed in the defect area, achieving robust mechanical and biological dual healing. Quantitative bone morphometric analysis (Figure 6D–F) revealed deeper differences in osteogenic efficacy. Although there was no statistical difference in BMD (Figure 6F) between the RBCP and 3D-SMPT groups, indicating that the newly formed bone induced by both was similar in mineralization quality, the 3D-SMPT group was considerably superior to the RBCP group and the control group in terms of both BV (Figure 6D) and BV/TV (Figure 6E). This result clearly demonstrates that, in restoring deficiencies in weight-bearing bones, the rigid mechanical support provided by 3D-SMPT effectively prevents spatial collapse of the defect area, thereby creating an extremely stable and superior microenvironment for the continuous ingrowth of a large volume of new bone tissue.

3.6. Histological evaluation of *in vivo* bone repair in the beagle dog model

The decalcified specimens were subjected to histological analyses, such as H&E and Masson's trichrome staining, at 12 weeks post-operation to be able to further verify the mineralization quality of the newly formed bone and the biological integration at the microscopic cellular and tissue levels. The histomorphology results were remarkably consistent with the aforementioned macroscopic radiological findings. As demonstrated in Figure 7A and 7B, the massive bone defect in the control group remained unhealed, with the central defect area predominantly occupied by abundant loose fibrous connective tissue. Microscopically, this confirmed a typical fibrous non-union outcome, with only isolated islands of new bone appearing at the margins next to the host bone stumps.

The overall tissue architecture in the RBCP group was extremely disordered, despite some new bone formation around the remaining ceramic implants. Echoing the structural collapse revealed in the CT scans, the RBCP scaffolds exhibited severe mechanical fragmentation and loss of continuity in the histological sections. Additionally, Masson's trichrome staining revealed that the collagen matrix of the new bone (stained blue) was fragmented and irregularly distributed among the ceramic debris, thereby failing to establish a coherent and effective biomechanical support network.

In sharp contrast, the 3D-SMPT group demonstrated exemplary osteogenic efficacy and outstanding osseointegration. Across various magnifications, the grid topology of the 3D-printed porous titanium scaffold (implants, black opaque areas) remained intact. High-magnification H&E images (Figure 7A, 10× and 20×) clearly displayed that abundant, densely packed eosinophilic new bone matrix (pink) had not only grown deeply into the 3D porous network but was also tightly apposed to the titanium surfaces, with no fibrous tissue ingrowth or encapsulation noted at the bone-implant interface. Furthermore, Masson's trichrome staining (Figure 7B, 20×) verified that the newly formed bone within the pores was deposited with abundant, highly organized, and mature collagen fibers (stained deep blue), marking that the regenerated bone tissue had entered an advanced stage of mineralization and remodeling.

Taken together, the comprehensive histological analyses demonstrate that the robust mechanical framework of 3D-SMPT effectively withstands the stresses of the *in vivo* weight-bearing environment, creating an irreplaceable and superior microenvironment for the development of strong bone–metal contact and the ongoing regeneration of substantial amounts of mature bone tissue.

4. Discussion

To date, effectively repairing critical-sized, load-bearing bone defects—which exceed 2 to 2.5 times the diameter of the bone and cannot heal spontaneously—remains a major clinical challenge in orthopedics.[43,44] The ideal bone

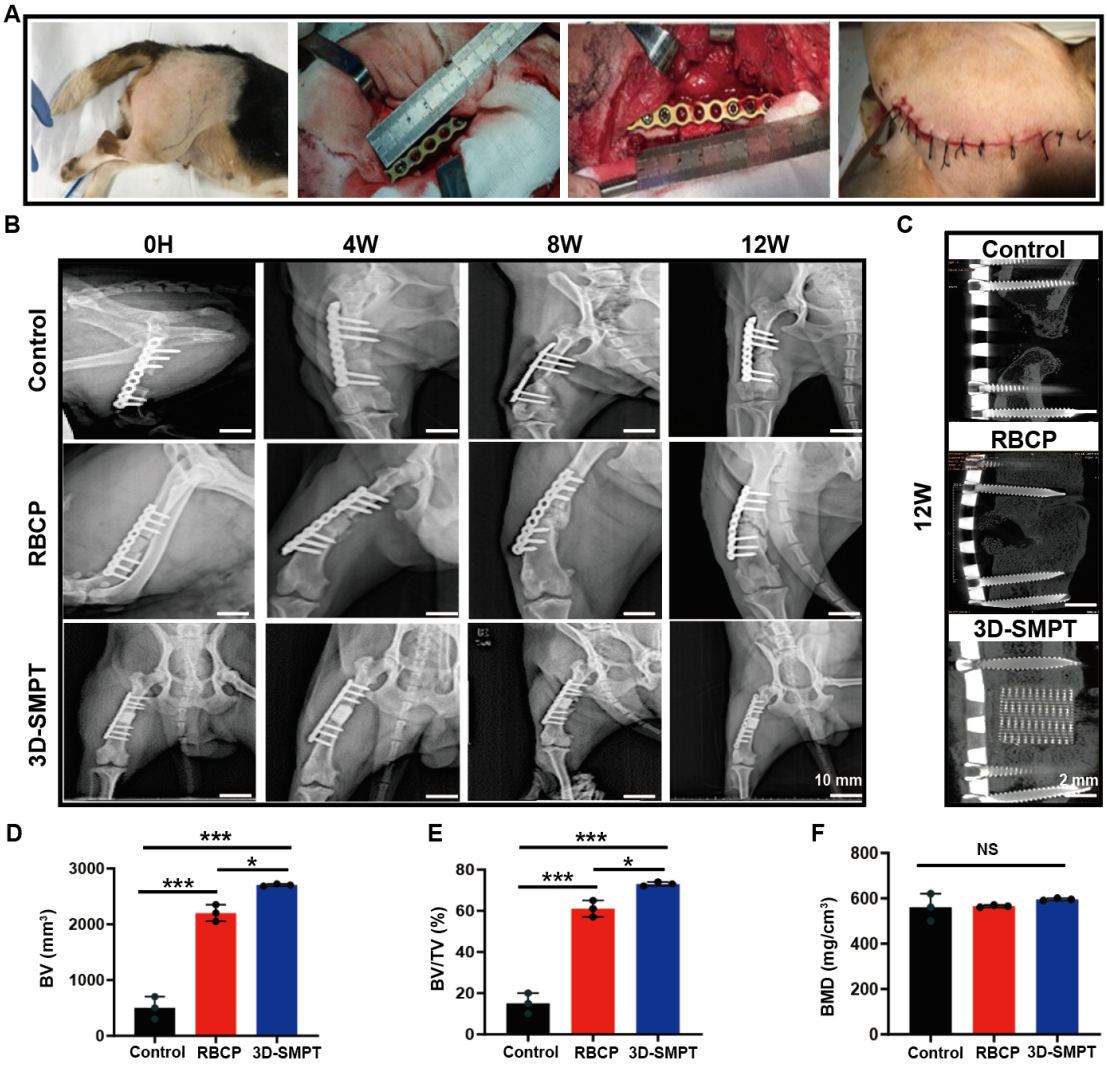

Figure 6. Radiological and micro-computed tomography (CT) evaluation of *in vivo* bone repair in a beagle dog model. (A) Macroscopic surgical photographs illustrating the creation of the critical-sized femoral defect, application of the internal fixation plate, and implantation of the scaffolds. (B) Radiographic images tracking the bone healing progression of each group at different postoperative time points (0H, 4W, 8W, and 12W). Scale bar: 10 mm. (C) Micro-CT two-dimensional slice images showing the new bone ingrowth and implant integrity within the defect area 12 weeks following surgery. Scale bar: 2 mm. (D–F) Bone volume (BV), bone volume fraction (BV/TV), and bone mineral density (BMD) quantitative micro-CT examination of the regenerated bone 12 weeks after surgery. Mean ± standard deviation ($n = 3$) is employed to express the data. *$p < 0.05$, ***$p < 0.001$; NS denotes no significant difference.

Abbreviations: 3D-SMPT: Surface-microstructured three-dimensional-printed porous titanium; RBCP: Reinforced biphasic calcium phosphate.

repair scaffold should exhibit superior osteoinductivity while delivering sustained and rigid mechanical support throughout the entire bone healing process.[45,46] To address this challenge, our study systematically and comprehensively compared the bone-regeneration efficacy of 3D-SMPT and RBCP ceramics, integrating *in vitro* cytological assessments with two *in vivo* animal models featuring distinct biomechanical gradients: a low weight-bearing rabbit ulnar model and a beagle femoral model that closely mimics human physiological load-bearing conditions. Our results demonstrate that 3D-SMPT not only matches traditional high-quality bioceramics in bioactivity but also offers a decisive clinical-translational advantage in load-bearing mechanical stability.

The inherent biological inertness of metal implant surfaces is the primary obstacle to achieving early and robust osseointegration.[47,48] Numerous prior studies have conclusively demonstrated that the anatase phase, induced on titanium surfaces via acid–alkali treatments, can significantly enhance the micro- and nanoroughness and hydrophilicity of the material interface.[49-51] Furthermore,

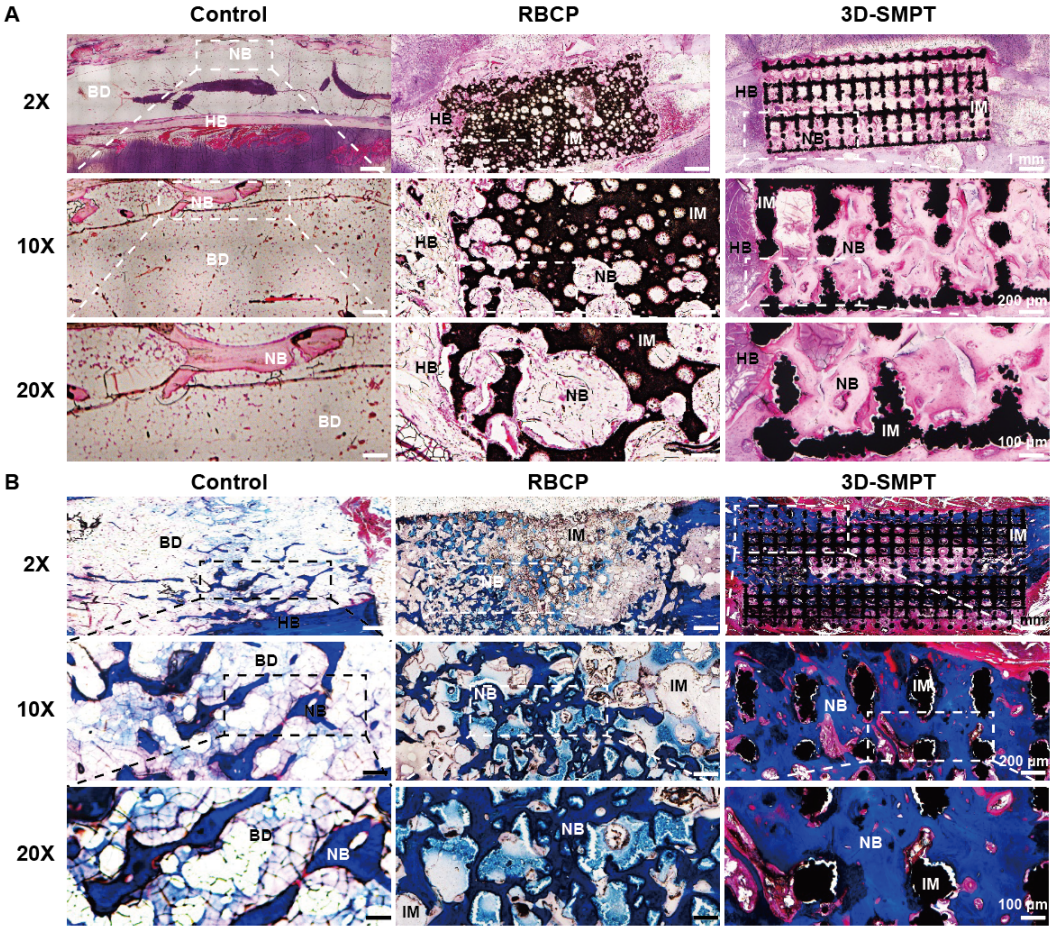

Figure 7. Histopathological assessment *in vivo*. (A) Newly produced bone at week 12 stained with hematoxylin and eosin. (B) Newly produced bone at week 12 stained with Masson. Scale bars of 1 mm, 200 μm, and 100 μm are shown by the magnifications of 2×, 10×, and 20×, respectively.
Abbreviations: 3D-SMPT: Surface-microstructured three-dimensional-printed porous titanium; BD: Bone defect; HB: Host bone; IM: Implant material; RBCP: Reinforced biphasic calcium phosphate.

subsequent modification with a HA coating—which closely mimics the inorganic composition of natural bone—represents one of the most effective strategies to overcome bioinertness and accelerate early osteogenic cell adhesion and differentiation.[52,53] Driven by this classical biomimetic surface-modification rationale, our study successfully constructed a microstructured composite coating containing both anatase and HA on the 3D-SMPT surface through combined acid–alkali treatment and electrochemical deposition. *In vitro* experiments confirmed that this surface modification conferred excellent biocompatibility on the titanium scaffolds, allowing BMSCs to spread fully. More importantly, 3D-SMPT demonstrated *in vitro* osteogenic effectiveness similar to that of the highly osteoinductive RBCP ceramics, significantly upregulating early ALP activity, late-stage development of mineralized nodules, and the transcriptional expression of core osteogenic genes (*OPN* and *OCN*). Mechanistically, the synergistic effect of the biomimetic HA coating and the rich micro- and nanotopography increased the number of protein adsorption sites, creating the ideal environment for osteogenic differentiation, cell adhesion, and proliferation.[54,55] These findings compellingly confirm that appropriately surface-activated porous titanium scaffolds can fully match, or even replace, traditional bioceramics in terms of early bioactivity.

Beyond the biomimetic surface-modification strategy employed in this study, recent advances in additive manufacturing have introduced a range of cutting-edge approaches for designing high-performance bone scaffolds. Among these, powder bed fusion, including selective laser melting, is the most widely used technique for fabricating titanium-based medical devices due to its ability to produce complex porous structures with

excellent mechanical properties.[56] For instance, advanced ceramic doping techniques—such as the incorporation of trace elements (e.g., strontium, magnesium, or silicon) into CaP-based scaffolds—have been shown to significantly enhance osteogenic activity and vascularization potential.[57] Similarly, the integration of bioactive glass into 3D-printed scaffolds offers the advantage of controlled ion release (e.g., silicon, calcium, phosphorus), which can stimulate osteoblast differentiation and extracellular matrix mineralization.[58,59] In parallel, multifunctional polymer composite systems that combine biodegradable polymers with inorganic nanofillers have emerged as promising platforms for achieving both tailored degradation rates and improved mechanical performance.[60] Furthermore, shape–memory scaffold designs, which enable minimally invasive implantation and dynamic mechanical stimulation of the surrounding tissue, represent a particularly innovative strategy for repairing complex bone defects.[61] Collectively, these emerging strategies underscore the growing diversity of functional scaffold architectures achievable through additive manufacturing. Compared with these approaches, our 3D-SMPT system achieves robust bioactivity through a purely surface–topography and HA-coating mechanism, without relying on ionic doping or polymer degradation. Nevertheless, future iterations of our scaffold design could benefit from incorporating bioactive glass coatings or exploring shape–memory mechanisms to further enhance osseointegration and enable controlled deployment in irregular defect sites.

The study's main finding is that the two scaffold materials function differently in different *in vivo* biomechanical settings. In the low weight-bearing rabbit ulnar critical-sized defect model, both 3D-SMPT and RBCP achieved excellent defect bridging, with no significant differences observed across key bone morphometric parameters (BMD, BV/TV, trabecular number). This suggests that in the absence of high mechanical stress, the osteoinductive capacities of the two materials are highly comparable. However, this equivalence was completely disrupted under high mechanical stress. While earlier research has shown that microstructural modification can partially enhance the mechanical properties of BCP ceramics, this improvement remains insufficient to meet the rigorous demands of massive load-bearing bone defect repair.[62,63] Indeed, when applied to the beagle femoral model, which closely mimics human anatomy and true load-bearing biomechanics, RBCP revealed the inherent, insurmountable brittleness of ceramic materials (with a compressive strength of only 7.68 MPa). As the animal's weight-bearing activities increased postoperatively, the RBCP scaffold suffered severe mechanical collapse and fragmentation *in vivo*. This mechanical failure not only led to the collapse of the local space for new bone formation but also caused stress to concentrate entirely on the internal fixation plate, ultimately resulting in plate bending and severe angular deformity of the affected limb. In sharp contrast, owing to its outstanding compressive strength of 83.14 MPa and the inherent non-degradability of titanium alloys, the 3D-SMPT scaffold maintained its macroscopic anatomical morphology and long-term stability throughout the entire healing period. For clinical context, it is worth noting that the compressive strength of human cortical bone ranges from approximately 88 to 193 MPa, while that of cancellous bone ranges from 2 to 12 MPa.[64] Thus, the 83.14 MPa achieved by 3D-SMPT falls within the lower range of cortical bone, making it highly suitable for load-bearing applications. It effectively shared the mechanical load of the internal fixation system, completely preventing repair failure caused by implant collapse or the loss of support due to premature degradation, thereby providing an extremely stable structural foundation for the continuous ingrowth of abundant new bone.

Furthermore, the excellent osseointegration demonstrated by 3D-SMPT at the micro-histological level is equally remarkable. Histological sections of the beagle femurs (H&E and Masson's trichrome staining) showed that the robust grid topology of 3D-SMPT maintained absolute integrity. A significant quantity of fully developed new bone, rich in highly organized collagen fibers, grew deeply into its 3D pores, and the bone–metal interface was tightly bonded without any fibrous tissue encapsulation. This ideal histological outcome is credited to the synergistic effect of the following advantages. First, the compressive strength of 3D-SMPT (83.14 MPa) is highly comparable to that of natural bone (88.3–193 MPa).[65,66] This, combined with its 66.0% porosity, substantially reduces the elastic modulus of the metal. This fundamentally mitigates bone resorption caused by the stress-shielding effect, laying a mechanical foundation for extending the long-term service life of the scaffold. Second, its interconnected 3D network provides ample space for massive vascular ingrowth and nutrient transport. Finally, its tough mechanical framework maintains a "micro-motion-free" microenvironment under complex *in vivo* stresses, which is crucial for osteoprogenitor cell differentiation and the bone remodeling process.

Although our findings have great clinical translational potential, it is crucial to recognize several limitations. The early- to mid-stage bone healing over a 12-week postoperative period was the main focus of this study. Therefore, extended follow-up observations are necessary to comprehensively assess the long-term performance of *in vivo* services, fatigue resistance, and the ongoing

biomechanical adaptation between the 3D-SMPT implant and the host bone. To further clarify the precise molecular pathways and methods by which the 3D-SMPT surface microstructures facilitate osteogenesis–angiogenesis coupling, we intend to incorporate transcriptomics or single-cell sequencing technologies in subsequent investigations. Additionally, it is important to acknowledge that unlike biodegradable CaP ceramics (e.g., RBCP), titanium is non-degradable. While this non-degradability provides sustained mechanical support essential for load-bearing applications, it also means that the 3D-SMPT scaffold will remain as a permanent implant *in vivo*. Clinically, this implies a potential risk of long-term foreign body response, stress-shielding-induced bone resorption over extended periods, and the need for secondary removal surgery if complications arise. Therefore, future efforts should focus on developing surface modifications or hybrid strategies that further enhance long-term biocompatibility and reduce potential adverse effects associated with permanent metallic implants.

In summary, 3D-SMPT not only effectively overcomes the inherent biological inertness of titanium but also resolves the critical clinical limitation of traditional CaP ceramics—their susceptibility to mechanical failure in load-bearing environments. With its exceptional biocompatibility, robust osteoinductive activity, and outstanding mechanical stability, 3D-SMPT can repair massive load-bearing bone defects and shows great promise for clinical use.

5. Conclusion

In summary, this study successfully engineered 3D-SMPT scaffolds and comprehensively validated their exceptional efficacy in reconstructing massive load-bearing bone defects. *In vitro*, the biomimetic coating successfully overcame the biological inertness of titanium, endowing 3D-SMPT with outstanding biocompatibility and osteoinductivity that parallel traditional premium RBCP ceramics. Crucially, *in vivo* cross-species evaluations across distinct biomechanical gradients revealed a stark contrast. While both scaffolds exhibited equivalent osteogenesis in a low-load environment (rabbit ulna), the highly biomimetic weight-bearing model (beagle femur) revealed the fatal brittleness of RBCP, leading to severe mechanical failure. Conversely, relying on its cortical bone-matched compressive strength (83.14 MPa), interconnected porosity, and anti-degradation properties, 3D-SMPT preserved absolute long-term mechanical stability. It successfully alleviated stress shielding, facilitating the deep ingrowth of abundant mature bone and achieving robust osseointegration. Ultimately, 3D-SMPT achieves a perfect integration of bioactivity and load-bearing stability, providing a highly promising clinical alternative for the repair of massive load-bearing bone defects.

Acknowledgments

The authors would like to thank the Northwest Institute for Non-ferrous Metal Research and the National Engineering Research Center for Biomaterials, Sichuan University, for providing the raw materials used in this study.

Funding

This research was funded by the National Natural Science Foundation of China (grant numbers 82372401 and 82272455) and the Beijing Natural Science Foundation (L256032).

Conflict of interest

The authors declare they have no competing interests.

Author contributions

Conceptualization: Xiao Liu, Hufei Wang, Jianpeng Gao, Jianheng Liu

Investigation: Jianheng Liu, Ming Li, Hua Chen, Zhengyang Chang, Jiazhi Yan

Funding acquisition: Jianheng Liu, Hufei Wang, Hua Chen

Writing–original draft: Zijian Li, Chenliang Quan

Writing–review & editing: Guanglin Wang, Hufei Wang

Ethics approval and consent to participate

Animal experiments in this study were approved by the Ethics Committee of PLA General Hospital (Approval No.: 2022-x18-51).

Consent for publication

Not applicable.

Availability of data

Data are available from the corresponding author upon reasonable request.

References

1. Wu AM, Bisignano C, James SL, *et al*. Global, regional, and national burden of bone fractures in 204 countries and territories, 1990-2019: a systematic analysis from the Global Burden of Disease Study 2019. *Lancet Healthy Longev*. 2021;2(9):e580-e592.

   doi: 10.1016/s2666-7568(21)00172-0

2. Migliorini F, La Padula G, Torsiello E, Spiezia F, Oliva F, Maffulli N. Strategies for large bone defect reconstruction after trauma, infections or tumour excision: a comprehensive review of the literature. *Eur J Med Res*. 2021;26(1):118.

doi: 10.1186/s40001-021-00593-9

3. Taiwo BS, Okoye PC, Rayner A, Guryel E, Robertson A. Minding the gap: management of bone defects after trauma. *Orthop Trauma*. 2025;39(5):295-301.

   doi: 10.1016/j.mporth.2025.08.005

4. Arealis G, Nikolaou VS. Bone printing: new frontiers in the treatment of bone defects. *Injury*. 2015;46:S20-S22.

   doi: 10.1016/S0020-1383(15)30050-4

5. Hao S, Wang F, Huang J, *et al*. Periosteum Organoid: Biomimetic Design Inspired From the Bone Healing Process. *Exploration*. 2025;5(6):20240298.

   doi: 10.1002/EXP.20240298

6. Smith CA, Richardson SM, Eagle MJ, Rooney P, Board T, Hoyland JA. The use of a novel bone allograft wash process to generate a biocompatible, mechanically stable and osteoinductive biological scaffold for use in bone tissue engineering. *J Tissue Eng Regen Med*. 2015;9(5):595-604.

   doi: 10.1002/term.1934

7. Dumic-Cule I, Pecina M, Jelic M, *et al*. Biological aspects of segmental bone defects management. *Int Orthop*. 2015;39(5):1005-1011.

   doi: 10.1007/s00264-015-2728-4

8. Hofmann GH, Sarsour R, Deursen Wv, *et al*. Immune rejection of orthopedic tissue allograft scoping review: Are we missing a cause of graft/procedural failure? Current concepts. *J ISAKOS*. 2025;15:101002.

   doi: 10.1016/j.jisako.2025.101002

9. Gao J, Wang H, Li M, *et al*. DLP-printed GelMA-PMAA scaffold for bone regeneration through endochondral ossification. *Int J Bioprint*. 2023;9(5):754.

   doi: 10.18063/ijb.754

10. Alonzo M, Primo FA, Kumar SA, *et al*. Bone tissue engineering techniques, advances and scaffolds for treatment of bone defects. *Curr Opin Biomed Eng*. 2021;17:100248.

    doi: 10.1016/j.cobme.2020.100248

11. Chen Y, Hu H, Wang D, *et al*. 2D copper nanozyme patches facilitate bone regeneration via interfacial modulation of osteoclast-osteoblast dynamics. *BMEMat*. 2026.

    doi: 10.1002/bmm2.70067

12. Tao Z, Yuan Z, Zhou D, *et al*. Fabrication of magnesium-doped porous polylactic acid microsphere for bone regeneration. *Biomater Transl*. 2023;4(4):280-290.

    doi: 10.12336/biomatertransl.2023.04.007

13. Qu Y, Wang Yn, Kong W, *et al*. 3D-printed nano-hydroxyapatite/polylactic acid scaffold with simvastatin-loaded hydroxyethyl methacrylate/sulfobetaine methacrylate hydrogel for accelerated bone repair. *Int J Bioprint*. 2026;12(1):025490505.

    doi: 10.36922/ijb025490505

14. Hou X, Zhang L, Zhou Z, *et al*. Calcium Phosphate-Based Biomaterials for Bone Repair. *J Funct Biomater*. 2022;13(4):187.

    doi: 10.3390/jfb13040187

15. Wang P, Zhao L, Liu J, Weir MD, Zhou X, Xu HHK. Bone tissue engineering via nanostructured calcium phosphate biomaterials and stem cells. *Bone Res*. 2014;2(1):14017.

    doi: 10.1038/boneres.2014.17

16. Jansen JA. Editorial: Calcium Phosphate Ceramics: The Living Bridge Between Biology and Biomaterials. *Tissue Eng Part C Methods*. 2025;31(11):381-383.

    doi: 10.1177/19373384251397945

17. Lu J, Yu H, Chen C. Biological properties of calcium phosphate biomaterials for bone repair: a review. *RSC Adv*. 2018;8(4):2015-2033.

    doi: 10.1039/C7RA11278E

18. Tang H, Zhao G, Lv Y, *et al*. Immunomodulatory 3D-printed hydroxyapatite/tricalcium phosphate/polycaprolactone scaffolds promote bone regeneration via macrophage polarization. *Int J Bioprint*. 2026;12(2):026060049.

    doi: 10.36922/ijb026060049

19. Tang Z, Tan Y, Ni Y, *et al*. Comparison of ectopic bone formation process induced by four calcium phosphate ceramics in mice. *Mater Sci Eng C Mater Biol Appl*. 2017;70(Pt 2):1000-1010.

    doi: 10.1016/j.msec.2016.06.097

20. Hu X, Zhang Z, Ning L, *et al*. Three-dimensional-printed bionic dual crosslinked drug-loaded hydrogel composite scaffolds for large bone defect repair. *Int J Bioprint*. 2025;12(1):348-370.

    doi: 10.36922/ijb025380391

21. Stempels HW, Lehr AM, Delawi D, *et al*. Efficacy of Biphasic Calcium Phosphate Ceramic With a Needle-Shaped Surface Topography Versus Autograft in Instrumented Posterolateral Spinal Fusion. *Spine*. 2024;49(19):1323-1331.

    doi: 10.1097/brs.0000000000005075

22. Zhu Y, Zhang K, Zhao R, *et al*. Bone regeneration with micro/nano hybrid-structured biphasic calcium phosphate bioceramics at segmental bone defect and the induced immunoregulation of MSCs. *Biomaterials*. 2017;147:133-144.

    doi: 10.1016/j.biomaterials.2017.09.018

23. Yang J, Chen HJ, Zhu XD, *et al*. Enhanced repair of a critical-sized segmental bone defect in rabbit femur by surface microstructured porous titanium. *J Mater Sci Mater Med*. 2014;25(7):1747-1756.

    doi: 10.1007/s10856-014-5202-8

24. Gavalda-Diaz O, Saiz E, Chevalier J, Bouville F. Toughening of ceramics and ceramic composites through microstructure engineering: A review. *Int Mater Rev*. 2025;70(1):3-30.

    doi: 10.1177/09506608241308337

25. Cai W, Huo Y, Liu Y, *et al*. Biomechanics in bone regeneration and mechanobiology in osteoblasts: Fundamental concepts and recent progress. *EngMedicine*. 2025;2(1):100057.

    doi: 10.1016/j.engmed.2025.100057

26. Thanigaivel S, Priya AK, Balakrishnan D, Dutta K, Rajendran S, Soto-Moscoso M. Insight on recent development in metallic biomaterials: Strategies involving synthesis, types and surface modification for advanced therapeutic and biomedical applications. *Biochem Eng J*. 2022;187:108522.

    doi: 10.1016/j.bej.2022.108522

27. Liu S, Manshaii F, Chen J, *et al*. Unleashing the Potential of Electroactive Hybrid Biomaterials and Self-Powered Systems for Bone Therapeutics. *Nano-Micro Lett*. 2024;17(1):44.

    doi: 10.1007/s40820-024-01536-9

28. Abd-Elaziem W, Darwish MA, Hamada A, Daoush WM. Titanium-Based alloys and composites for orthopedic implants Applications: A comprehensive review. *Mater Des*. 2024;241:112850.

    doi: 10.1016/j.matdes.2024.112850

29. Chen C, Xie Z, Yang S, *et al*. Machine Learning Approach to Investigating Macrophage Polarization on Various Titanium Surface Characteristics. *BME Front*. 2025;6:0100.

    doi: 10.34133/bmef.0100

30. Fan S, Li S, Wu Y, *et al*. Customized 3D-printed heterogeneous porous titanium scaffolds for bone tissue engineering. *MedComm Biomater Appl*. 2024;3(2):e80.

    doi: 10.1002/mba2.80

31. Yuan B, Liu P, Zhao R, *et al*. Functionalized 3D-printed porous titanium scaffold induces in situ vascularized bone regeneration by orchestrating bone microenvironment. *J Mater Sci Technol*. 2023;153:92-105.

    doi: 10.1016/j.jmst.2022.12.033

32. Takemoto M, Fujibayashi S, Neo M, Suzuki J, Kokubo T, Nakamura T. Mechanical properties and osteoconductivity of porous bioactive titanium. *Biomaterials*. 2005;26(30):6014-6023.

    doi: 10.1016/j.biomaterials.2005.03.019

33. Dunand DC. Processing of Titanium Foams. *Adv Eng Mater*. 2004;6(6):369-376.

    doi: 10.1002/adem.200405576

34. Hao P, Liu J, Zhang C, Lyu L. Design of the Elastic Modulus of porous lattice structures composed of cells with continuously variable cross section carrying structures. *Clin Biomech*. 2024;119:106330.

    doi: 10.1016/j.clinbiomech.2024.106330

35. Luo B, Miu L, Luo Y. Titanium alloys for biomedical applications: a review on additive manufacturing process and surface modification technology. *Int J Adv Manuf Technol*. 2025;137(7-8):3215-3227.

    doi: 10.1007/s00170-025-15287-3

36. Wang XX, Hayakawa S, Tsuru K, Osaka A. Improvement of bioactivity of H2O2/TaCl5-treated titanium after subsequent heat treatments. *J Biomed Mater Res*. 2000;52(1):171-176.

    doi: 10.1002/1097-4636(200010)52:1<171::AID-JBM22>3.0.CO;2-O

37. Yang J, Wang J, Yuan T, *et al*. The enhanced effect of surface microstructured porous titanium on adhesion and osteoblastic differentiation of mesenchymal stem cells. *J Mater Sci Mater Med*. 2013;24(9):2235-2246.

    doi: 10.1007/s10856-013-4976-4

38. Liu X, Gao J, Liu J, *et al*. Three-Dimensional-Printed Spherical Hollow Structural Scaffolds for Guiding Critical-Sized Bone Regeneration. *ACS Biomater Sci Eng*. 2024;10(4):2581-2594.

    doi: 10.1021/acsbiomaterials.3c01956

39. Liu X, Chang Z, Li Z, *et al*. Hollow spherical mineralized scaffold integrated with a bone marrow mesenchymal stem cell-laden three-dimensional delivery system for regeneration of critical-sized bone defects. *Int J Bioprint*. 2026;12(2):026050046.

    doi: 10.36922/ijb026050046

40. Qing F, Wang Z, Hong Y, *et al*. Selective effects of hydroxyapatite nanoparticles on osteosarcoma cells and osteoblasts. *J Mater Sci Mater Med*. 2012;23(9):2245-2251.

    doi: 10.1007/s10856-012-4703-6

41. Heise T, Sawyer AY, Hirai T, Schaible S, Sy H, Wickramasekara S. Report on investigation of ISO 10993–12 extraction conditions. *Regul Toxicol Pharmacol*. 2022;131:105164.

    doi: 10.1016/j.yrtph.2022.105164

42. Kovrlija I, Menshikh K, Abreu H, *et al*. Corrigendum to "Challenging applicability of ISO 10993-5 for calcium phosphate biomaterials evaluation: Towards more accurate in vitro cytotoxicity assessment" [Biomater. Adv. 160 (2024) 213866]. *Biomater Adv*. 2025;177:214386.

    doi: 10.1016/j.bioadv.2025.214386

43. Yu D, Shen W, Dai J, Zhu H. Treatment of large bone defects in load-bearing bone: traditional and novel bone grafts. *J Zhejiang Univ Sci B*. 2025;26(5):421-447.

    doi: 10.1631/jzus.B2300669

44. Reichert JC, Saifzadeh S, Wullschleger ME, *et al*. The challenge of establishing preclinical models for segmental bone defect research. *Biomaterials*. 2009;30(12):2149-2163.

    doi: 10.1016/j.biomaterials.2008.12.050

45. Jiang S, Wang M, He J. A review of biomimetic scaffolds for bone regeneration: Toward a cell-free strategy. *Bioeng Transl Med*. 2021;6(2):e10206.

doi: 10.1002/btm2.10206

46. Todd EA, Mirsky NA, Silva BLG, *et al*. Functional Scaffolds for Bone Tissue Regeneration: A Comprehensive Review of Materials, Methods, and Future Directions. *J Funct Biomater*. 2024;15(10):280.

doi: 10.3390/jfb15100280

47. Chen Q, Gu J, Zhang H, *et al*. Promoting implant osseointegration via the osteoblast-selective β-amino acid polymer strategy. *Nat Commun*. 2025;16(1).

doi: 10.1038/s41467-025-58394-1

48. Cheng X, Yang X, Liu C, *et al*. Stabilization of Apatite Coatings on PPENK Surfaces by Mechanical Interlocking to Promote Bioactivity and Osseointegration In Vivo. *ACS Appl Mater Interfaces*. 2023;15(1):697-710.

doi: 10.1021/acsami.2c20633

49. Chang L, Chen P, Mokudai T, Kawashita M, Mizoguchi I, Kanetaka H. Enhancing Titanium Osteoconductivity by Alkali-Hot Water Treatment. *ACS Omega*. 2024;9(44):44568-44576.

doi: 10.1021/acsomega.4c06702

50. Tuikampee S, Chaijareenont P, Rungsiyakull P, Yavirach A. Titanium Surface Modification Techniques to Enhance Osteoblasts and Bone Formation for Dental Implants: A Narrative Review on Current Advances. *Metals*. 2024;14(5):515.

doi: 10.3390/met14050515

51. Ruan D, Wu C, Deng S, Zhang Y, Guan G. The Anatase Phase of Nanotopography Titania with Higher Roughness Has Better Biocompatibility in Osteoblast Cell Morphology and Proliferation. *Biomed Res Int*. 2020;2020(1):8032718.

doi: 10.1155/2020/8032718

52. Arcos D, Vallet-Regí M. Substituted hydroxyapatite coatings of bone implants. *J Mater Chem B*. 2020;8(9):1781-1800.

doi: 10.1039/c9tb02710f

53. Liu W, Cheong N, He Z, Zhang T. Application of Hydroxyapatite Composites in Bone Tissue Engineering: A Review. *J Funct Biomater*. 2025;16(4):127.

doi: 10.3390/jfb16040127

54. Zhang W, Wang G, Liu Y, *et al*. The synergistic effect of hierarchical micro/nano-topography and bioactive ions for enhanced osseointegration. *Biomaterials*. 2013;34(13):3184-3195.

doi: 10.1016/j.biomaterials.2013.01.008

55. Duan G, Chang D, Zhang C, *et al*. Biofunctionalisation strategies of material surface and the inspired biological effects for bone repair. *Biosurf Biotribol*. 2024;10(2):17-41.

doi: 10.1049/bsb2.12081

56. Ng WL, An J, Chua CK. Process, Material, and Regulatory Considerations for 3D Printed Medical Devices and Tissue Constructs. *Engineering*. 2024;36:146-166.

doi: 10.1016/j.eng.2024.01.028

57. Guo W, Li P, Wei Y, *et al*. Ionic substitution through bredigite doping for microstructure and performance adjustment in DLP 3D-printed TPMS porous HA bone scaffolds. *Virtual Phys Prototyp*. 2024;19(1):e2423840.

doi: 10.1080/17452759.2024.2423840

58. Xu Z, Qi X, Bao M, *et al*. Biomineralization inspired 3D printed bioactive glass nanocomposite scaffolds orchestrate diabetic bone regeneration by remodeling micromilieu. *Bioact Mater*. 2023;25:239-255.

doi: 10.1016/j.bioactmat.2023.01.024

59. Bergoglio M, Najmi Z, Cochis A, Miola M, Vernè E, Sangermano M. Silanized and Cu-doped bioactive glass as filler for biobased photocurable 3D printed scaffolds. *Mater Today Chem*. 2025;44:102559.

doi: 10.1016/j.mtchem.2025.102559

60. Ganeshkumar S, Rahman HA, Gowtham TM, Adithya T, Suyambulinagm I, Maniraj J. Multifunctional Polymer Composites: Design, Properties, and Emerging Applications—A Critical Review. In: *Springer Proceedings in Materials*. Singapore: Springer Nature Singapore; 2024:637-649.

doi: 10.1007/978-981-97-7071-7_45

61. Pu Z, Gong W, Wu H, *et al*. Innovative applications and future challenges of shape memory scaffolds for functional reconstruction in diseases of the musculoskeletal system. *Colloids Surf B Biointerfaces*. 2026;261:115426.

doi: 10.1016/j.colsurfb.2026.115426

62. Dong D, Su H, Li X, *et al*. Microstructures and mechanical properties of biphasic calcium phosphate bioceramics fabricated by SLA 3D printing. *J Manuf Process*. 2022;81:433-443.

doi: 10.1016/j.jmapro.2022.07.016

63. Miri Z, Haugen HJ, Loca D, *et al*. Review on the strategies to improve the mechanical strength of highly porous bone bioceramic scaffolds. *J Eur Ceram Soc*. 2024;44(1):23-42.

doi: 10.1016/j.jeurceramsoc.2023.09.003

64. Rohlmann A, Zilch H, Bergmann G, Kölbel R. Material properties of femoral cancellous bone in axial loading. Part I: Time independent properties. *Arch Orthop Trauma Surg*. 1980;97(2):95-102.

doi: 10.1007/bf00450930

65. Wu Y, Li M, Su H, Chen H, Zhu Y. Up-to-date progress in

bioprinting of bone tissue. *Int J Bioprint*. 2023;9(1):628.
doi: 10.18063/ijb.v9i1.628

66. Bose S, Roy M, Bandyopadhyay A. Recent advances in bone tissue engineering scaffolds. *Trends Biotechnol*. 2012;30(10):546-554.
doi: 10.1016/j.tibtech.2012.07.005